Ocean Dynamics (2012) 62:753–769
DOI 10.1007/s10236-011-0517-1

M_2 tidal dynamics in Bohai and Yellow Seas: a hybrid data assimilative modeling study

Zhigang Yao · Ruoying He · Xianwen Bao · Dexing Wu · Jun Song

Received: 30 August 2011 / Accepted: 21 December 2011 / Published online: 3 February 2012

Abstract A high-resolution hybrid data assimilative (DA) modeling system is adapted to study the M_2 barotropic tidal characteristics and dynamics in the Bohai and Yellow Seas. In situ data include tidal harmonics extracted from both coastal sea level and bottom pressure observations. The hybrid DA system consists of both forward and inverse models. The former is three-dimensional, finite-difference, nonlinear Regional Ocean Modeling System (ROMS). The latter is a three-dimensional, linearized, frequency-domain, finite-element model TRUXTON. The DA system assimilates in situ observations via the inversion of the barotropic tidal open boundary conditions (OBCs). Model skill is evaluated by comparing misfits between the observed and modeled tidal harmonics. The assimilation scheme is found effective and efficient in correcting the tidal OBCs, which in turn improves ROMS tidal solutions. Up to 50% reduction of model/data misfits is achieved after data assimilation. M_2 co-tidal maps constructed from the posterior (data assimilative) ROMS solutions agree well with observational analysis of (Fang et al. 2004). Detailed analyses on tidal mixing, residual current, energy flux, dissipation, and momentum term balance dynamics are performed for M_2 constituent, revealing complex M_2 tidal characteristics in the study region and the important role of coastal geometry and topography in affecting regional tidal dynamics.

Keywords Tidal inversion · Boundary conditions · Hybrid data assimilation · Refining

Responsible Editor: Jarle Berntsen

This article is part of the Topical Collection on the *3rd International Workshop on Modelling the Ocean 2011*

Z. Yao · X. Bao · D. Wu
College of Physical and Environmental Oceanography,
Ocean University of China,
Qingdao 266100, China

Z. Yao · R. He (✉)
Department of Marine, Earth and Atmospheric Sciences,
North Carolina State University,
Raleigh, NC 27695, USA
e-mail: rhe@ncsu.edu

Z. Yao · X. Bao · J. Song
Key Laboratory of Physical Oceanography,
Ocean University of China,
Qingdao 266100, China

J. Song
National Marine Data and Information Service,
State Oceanic Administration,
Tianjin 300171, China

1 Introduction

The Bohai and Yellow Seas are relatively flat continental shelf embayments surrounded by mainland China and Korean Peninsula (Fig. 1). The water depth is shallow, ranging from 20 m near the coast to around 90 m in the middle of the Yellow Sea. The central Yellow Sea Trough runs across the south Yellow Sea in the NNW–SSE direction and then turns to nearly E–W direction in the north Yellow Sea, constituting the major topographic feature in this area.

Barotropic tides are the dominant circulation processes in the regional seas, having considerable amplitudes as well as momentum and energy fluxes. Earlier studies (Choi 1980; Choi et al. 2003; Fang et al. 2004; Larsen et al. 1985) showed that regional tidal characteristics have very complex structures, and because of the joint effects of both massive tidal energy flux input and enhanced bottom friction associated with shallow shelf topography, the dissipation of M_2 (the largest constituent) tidal energy is up to 180 GW in the area, accounting for

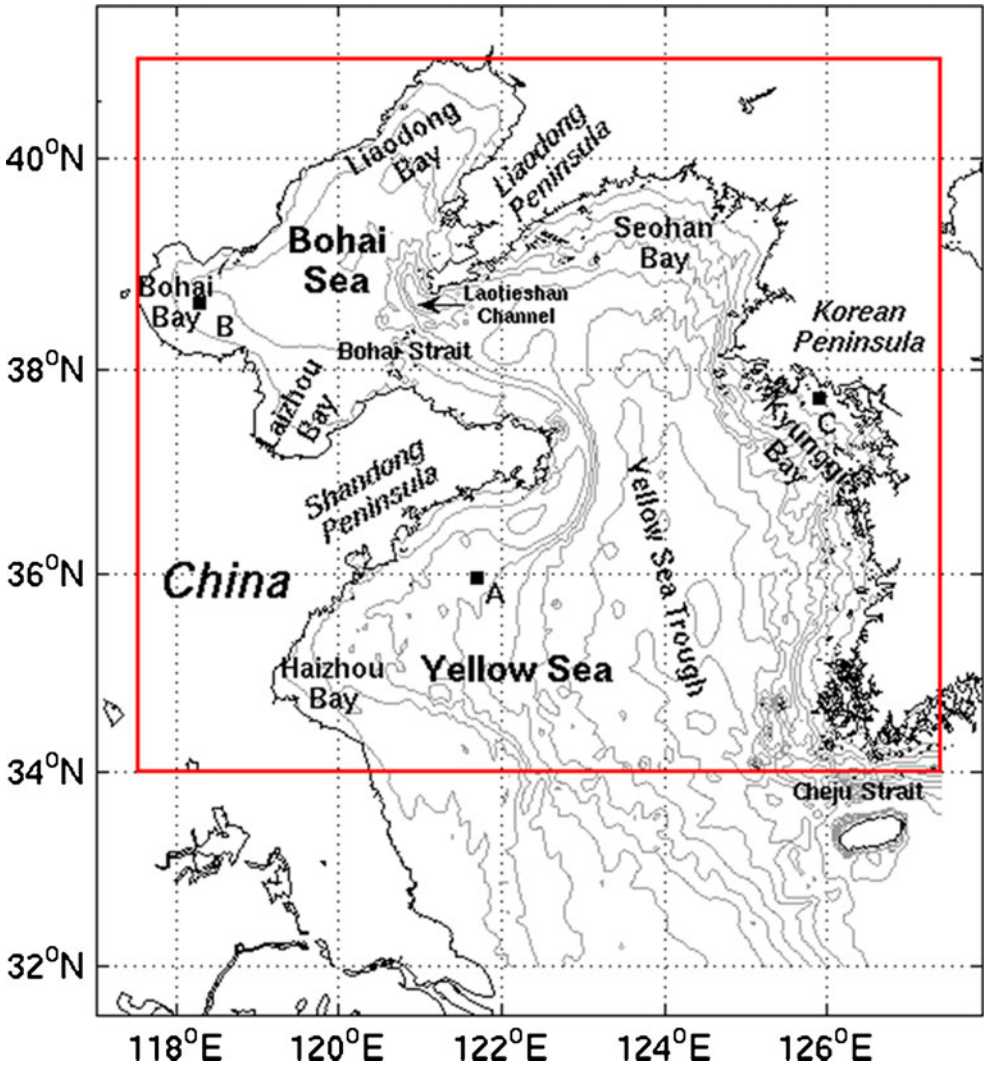

Fig. 1 Map of study region. *Gray contour lines* represent the bathymetry ranging from 10 to 90 m, with an interval of 10 m. A NNW–SSE-oriented Yellow Sea Trough runs across the southern part of Yellow Sea and then turns toward E–W direction in the northern part. Stations *A* to *C* are locations where momentum analysis is performed and discussed later in the paper. The model domain is plotted by the *red box*

approximately 11.1% of its global sums (i.e., 2TW) (Provost and Lyard 1997). Consequently, the tidal mixing and tidal residual currents play an important role in affecting many other physical and biogeochemical processes in this region. For instance, the vertical tidal mixing was proven to be a critical factor in the formation of the Yellow Sea Cold Water (Lu et al. 2009) and the development of a frontal structure in the Bohai Sea (Lie 1989), as well as the anchovy eggs distribution (Hao et al. 2003) and bacterial growth in the Yellow Sea (Hyun et al. 1999).

Regional tides and tidal dynamics were initially studied using limited sea level observations from coastal tidal gauges (Fang 1986, 1994; Ogura 1933). The advent of satellite altimetry provides open ocean sea level observations on routine basis, allowing for description of region-wide tidal characteristics (Fang et al. 2004). Numerical models (Choi 1980; Fang and Yang 1985; Kang et al. 1998; Lee and Jung 1999; Zhao et al. 1993) have also been used extensively to simulate and understand regional tidal dynamics. The effect of gravitational tidal potential is usually ignored for the region as the gravitational tides only account for around ~3% in the Yellow Sea (An 1977). Thus, most tidal models essentially solve the boundary value problem, and the principal challenge of modeling tides accurately is to properly represent tidal elevation and velocity boundary conditions around the model perimeter. The conventional way to achieve this is to use global/basin-scale tidal models to provide open boundary conditions (OBCs). Although significant progress has been made to advance global/basin-scale tidal models, and their solutions are fairly accurate in the open ocean and many shelf seas (e.g., [Shum et al. 1997]), they are often not so accurate in coastal regions that have complex coastlines and bathymetric features (such as the Yellow and Bohai Seas, (Lefevre et al. 2000)) due to limitations in their model resolutions and/or coarse bathymetric data being used. Direct use of the global or basin-scale tidal model solutions (harmonic constants) as OBCs therefore results in dynamical incompatibility and error accumulation that further degrade the utility of high-resolution regional tidal models. Techniques such as nudging method have been used to blend local observations

with regional model solutions to improve model performance at some coastal stations (Wang et al. 2004). But in most tidal model applications, the problem is approached by "fine tuning" tidal OBCs to minimize model observation misfits via the trial-and-error approach based on empirical experience.

Inverse data assimilation techniques were introduced as a more advanced method to systematically fine tune OBCs. Earlier examples in 2-D modeling framework include (McIntosh and Bennett 1984; Han et al. 2001; Lu and Fang 2002). An efficient inverse procedure to fine tune tidal OBCs for a 3-D south Atlantic Bight ocean model was later introduced by Lynch et al. (2004). The utility and effectiveness of this method were further demonstrated in the New England shelf tidal modeling application by He and Wilkin (2006).

Our objective here is to construct a similar inverse data assimilation tidal modeling system for the Yellow and Bohai Seas. The "best" OBCs resulted from assimilating observed coastal tidal harmonics are used to drive a high-resolution 3-dimensional regional ocean model to produce the optimal representation of regional tidal dynamics. For the proof of concept, we start with a simple setup that neglects a baroclinic effect (i.e., the density field is set to be homogeneous in the entire domain) and consider barotropic M_2 tide only as it is the most dominant tidal component in the Yellow and Bohai Seas (Bao et al. 2001; Choi 1980; Fang 1986, 1994).

The remainder of this paper is organized as follows. Section 2 gives a brief description of observational data used in the tidal inversion. The inverse data assimilation modeling system is described in Section 3. Inversion of open boundary conditions and model validation are discussed in Section 4. Regional M_2 tidal characteristics and dynamics are discussed in Section 5 and 6, respectively, followed by a summary and conclusion in Section 7.

2 Observations

In situ observations used in this study include 44 sets of tidal harmonics (Fig. 2) derived from an extensive collections of coastal tidal gauge and bottom pressure measurements, as well as published data from scientific journals. Among these, five sets are derived from sea level observations with temporal length varying from several years to more than two decades, therefore constituting an ideal data source for deriving tidal harmonics. These include two sets from the Korea Hydrographic and Ocean Administration observations (#42 and #43) located in the southern tip of the Korean Peninsula, three sets from the Chinese coastal tidal gauges (#8, #38, and #39).

The rest of the 39 sets of tidal harmonics are derived from various short-term sea level/bottom pressure observations.

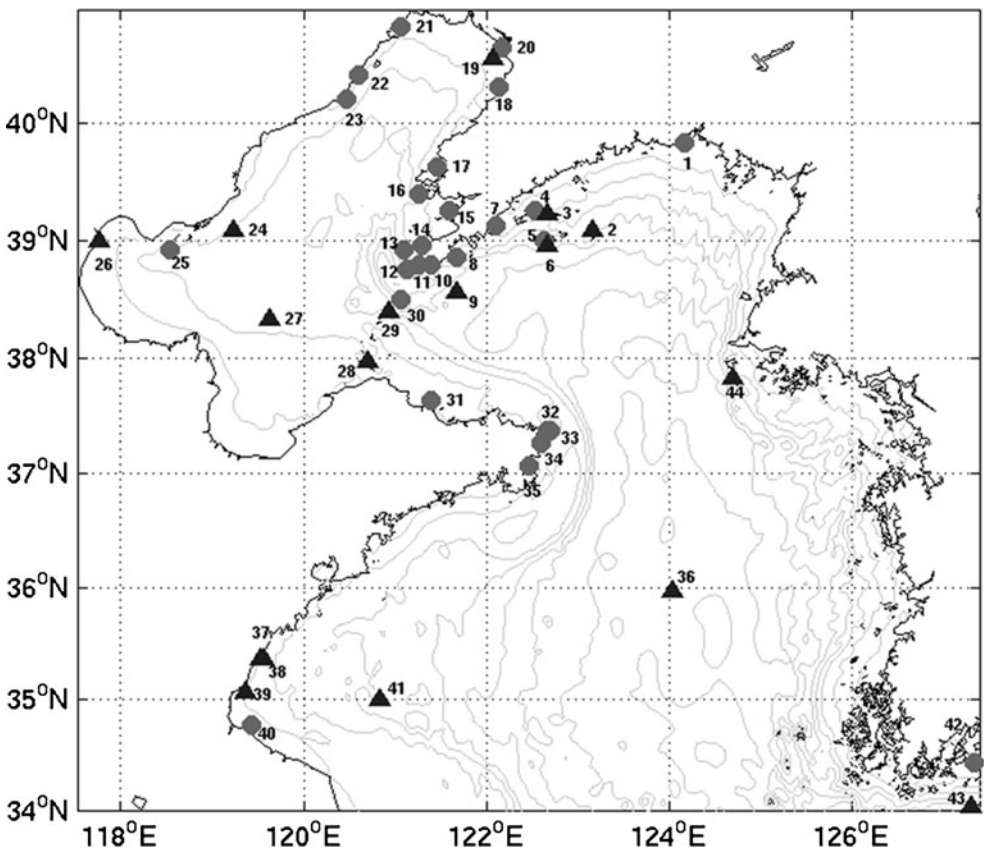

Fig. 2 Locations of tidal gauge and bottom pressure stations where tidal harmonic constants (*HC*) were derived. *Grey dots* indicate the active stations where HC were assimilated to drive inverse model, while *black triangles* represent passive stations for independent model skill assessment

The temporal length of these 39 short-term measurements varies from 1 month to several months. While not suitable to resolve all tidal constituents, they are sufficient to derive the M_2 constituent with a fairly good accuracy (Thomson and Emery 2001). Among them, ten sets (#2~6, #9, #27~30) are based on short-term bottom pressure observations in the middle of the Bohai and northern Yellow Seas during Comprehensive Investigation and Assessment of China Seas Project. Located in the middle of the southern Yellow Sea, tidal harmonics at #36 is taken from a previous study (Teague et al. 1998). The remaining 28 tidal gauge observations along the Chinese coastline come from routine observations by the Chinese State Oceanic Administration and historical data archive.

To extract the harmonic constants of M_2 constituent from these sea level/bottom pressure time series, we follow a standard least-square harmonics analysis procedure that incorporates nodal modulations, astronomical argument corrections, and inference calculations for tidal amplitude and phase (Foreman 1979; Pawlowicz et al. 2002). We purposely choose to use tidal harmonic constant observations from coastal tide gauge and bottom pressure observations because they are more accurate representations of barotropic tides than the current measurements, containing much less uncertainty introduced by small-scale bathymetric irregularity and oceanic processes.

We divide these sets into two groups. The first group includes 27 stations that are mainly distributed along the coast. We refer to these as the "active" stations (denoted as grey cycles in Fig. 2), which are used in data assimilation described below to drive an inverse model. The other group consists of 17 observations (denoted as black triangles in Fig. 2) scattered largely in the interior of our ocean domain. As such, they are good indicators to evaluate the model interior solutions. They are used only as the validation set and designated as "passive" stations.

3 Hybrid data assimilation system

The data assimilation system consists of both forward and inverse components. The forward model is the three-dimensional, hydrostatic primitive equation Regional Ocean Modeling System (ROMS). ROMS is a free-surface, finite difference circulation model, formulated in a vertical terrain-following sigma coordinate. The horizontal discretization is done on an orthogonal curvilinear Arakawa-C grid. Our regional ROMS implementation for the Bohai and Yellow Seas extends from 34° N to 42° N meridionally and from 117° E to 127.4° E zonally, and has a fine grid resolution of 2 min (1/30 degree). The model topography is extracted from global ETOPO2 dataset and further smoothed following a new approach by Sikiric et al. (2009) to increase model's stability and also retain local topographic features as realistic as possible. For open boundary conditions, we apply Orlanski-type radiation condition (Marchesiello et al. 2001) to the three-dimensional velocity. The free surface (ζ) and depth-averaged velocity (u) boundary conditions use the radiation method of Flather (1976), i.e.,

$$u = u_t + \sqrt{g/h}(\varsigma - \varsigma_t),$$

where g is the acceleration due to the earth gravity, h is the local water depth, and ζ_t and u_t are the estimations of tidal elevation and velocity boundary conditions to be specified, and thus are the objects of our "fine tuning."

The inverse component of our system is the three-dimensional linearized, sigma-coordinate finite element model TRUXTON (Lynch et al. 1998). Its discretization is harmonic in time and finite element in space. TRUXTON was originally constructed as the inverse of QUODDY, a three-dimensional nonlinear finite element forward circulation model (Lynch and Naimie 1993). The utility and effectiveness of TRUXTON in fitting QUODDY solutions to observations by deducing corrections to tidal OBCs have been demonstrated in modeling various coastal regions with different circulation settings, such as, the Gulf of Maine (He et al. 2005), Georges Bank (Aretxabaleta et al. 2005; Lynch et al. 1998), East China Sea (Naimie et al. 2001; Naimie and Lynch 2001), and the South Atlantic Bight (Lynch et al. 2004], to name a few. Mathematically, the inverse deduction is achieved by minimizing a quadratic cost function J in the least square sense**.** Let η represent the unknown boundary elevation adjustments to be estimated and ε are the model/data misfits. The quadratic cost function J is defined as:

$$J = \frac{1}{N_\eta \sigma_\eta^2} \sum_{i=1}^{N_\eta} \varepsilon^2 + w_0 \oint \eta^2 ds + w_1 \oint \left(\frac{\partial \eta}{\partial s}\right)^2 ds,$$

where σ_η is expected error of misfit ε, N_η is the numbers of observations, and ds denotes incremental distance along the model's open boundary. The first term on the right is the quadratic model/data misfit ε, which is defined as the complex difference between the observed and modeled tidal harmonics (i.e., tidal amplitude and phases in this case). The next two terms are the regularization terms, which penalize the size and spatial slope of boundary adjustment η to exert extra spatial constraint. w_0 and w_1 represent the inverse covariance of η and the elevation slope, respectively.

For this Bohai and Yellow Seas application, we choose expected size of elevation misfit to be 0.05 m, expected size of boundary adjustment as 0.05 m, and expected slope of boundary adjustment as 10^{-7}. These three metrics were all weighted equally in the minimization, and their values are consistent with the order of magnitude of prior estimates of these quantities. Since misfit ε can be supplied from any forward model by comparing model solutions to observations,

our premise is that by using TRUXTON and ROMS together, we can utilize interior observations to "fine-tune" ROMS tidal OBCs. The resulting hybrid data assimilation scheme therefore provides a better alternative to the commonly used, empirical "trial-and-error" approach.

The detailed hybrid assimilation procedure (Fig. 3) is as follows: (1) we start by running the ROMS forced by *prior* estimates of tidal open boundary conditions for a length of 30 days. This is based on Thomson and Emery (2001), which indicated that a length of a 30-day record is sufficient to resolve the M_2 tide focused herein. Hourly ROMS simulated elevations are saved and analyzed by harmonic fitting to derive tidal harmonics for M_2; (2) The misfits between the observed and modeled tidal harmonics at "active" stations are used to drive the TRUXTON to deduce corrections to the tidal boundary conditions, and (3) the adjustments are added to the prior OBCs to form more accurate *posterior* open boundary elevation and velocity specifications, which subsequently drive another forward ROMS run.

Although TRUXTON is a linearized inverse model, it retains the principal nonlinearity of the tidal system (i.e., the motion-dependent frictions and vertical turbulence viscosity) by using the mixing and bottom stress coefficients generated by the forward model (He and Wilkin 2006; Lynch et al. 1998). In this case, ROMS takes the 2.5 level Mellor–Yamada turbulence closure scheme, plus a quadratic bottom friction law based on the near-bottom velocity u_b ($\tau = C_d|u_b|u_b$, where C_d is the bottom friction coefficient, 0.003). The nonlinearity of the overall system requires the process to be iterated until no further significant improvement of the OBCs (or equivalently, further improvement in forward model solutions) is achieved. Our results show that two iterations are sufficient, as the largest inverse deduction occurring after the first inverse iteration.

It should be noted that because ROMS uses a structured rectangular grid, whereas TRUXTON use an unstructured triangle mesh, a prerequisite for using this hybrid data assimilative system is model gridding. To avoid potential inconsistency between the bathymetry and resolution of the two models, we purposely construct the unstructured mesh by directly subdividing the ROMS rectangle grid into triangles, thereby enhancing consistency of the two models. The TRXTON solutions at the unstructured nodes are then mapped to the ROMS boundary cells using nearest neighbor interpolation scheme with the assumption that within the ROMS 1/30 degree grid cell, variations in tidal amplitude and phase are negligible.

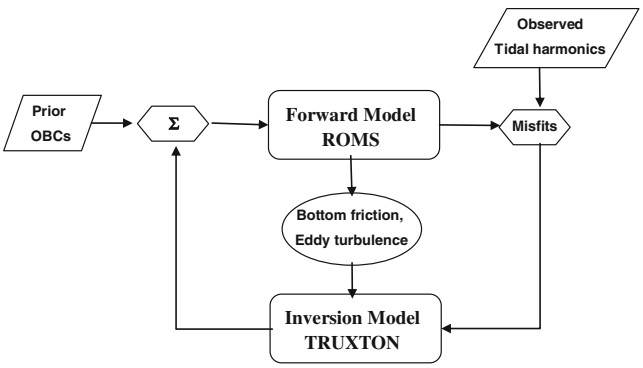

Fig. 3 Flow chart of hybrid data assimilation tidal modeling system

4 Regional tidal inverse solution and validation

The prior estimation of tidal open boundary conditions used for the Bohai and Yellow Seas ROMS was extracted from 1/30°China Sea regional tidal harmonic database of Oregon State University Tidal Data Inversion (OTIS) (Egbert et al. 1994; Egbert and Erofeeva 2002). OTIS tidal dataset has been extensively used and verified in previous applications over China Sea regions, such as in the Yellow Seas (Xia et al. 2006) and South China Sea (Zu et al. 2008).

By assimilating tidal harmonics from "active stations," inverse deduction provides incremental fine tuning of amplitude and phase distributions for tidal constituent along the ROMS open boundary during each of two inverse iterations. These data-inverted adjustments correct for the issues of "prior" OBCs, which as discussed earlier, largely come from the insufficiency of basin-scale tidal model and/or coarse bathymetric data being used. Differences between the prior and the final posterior tidal sea level boundary conditions highlight the impacts made by the inverse data assimilation (Fig. 4). The adjustments of tidal amplitude for M_2 along the open boundary ranges from −4.49 to 7.9 cm, which is about 10% of the total tidal amplitude. The general pattern of tidal amplitude corrections is characterized by an amplitude increase along the southern boundary and a decrease along the eastern boundary. The most significant correction occurs in the Subei Shoals off the coast of mainland China, where the tidal amplitude adjustment is up to 8 cm. Along the eastern boundary, data inversion provides less than 5 cm of correction in tidal amplitude. In terms of tidal phase, the adjustment ranges from −9.4° to 1.8° along the southern boundary, and about less than 2° along the eastern boundary.

Although these data-inverted adjustments seem small relative to the total tidal signals along the model's open boundaries, correcting these errors is important as they tend to amplify as the tidal waves approach shoreward. Moreover, these adjustments altogether are significant relative to the subtidal (e.g., wind-driven) sea level signal, which is on the order of 10 cm. This unfavorable signal-to-tide ratio makes it easy to smear the subtidal variability unless the tides are very precisely resolved and predicted. Hence, describing and understanding subtidal signal themselves call for the need for inverse deduction in the tidal bands.

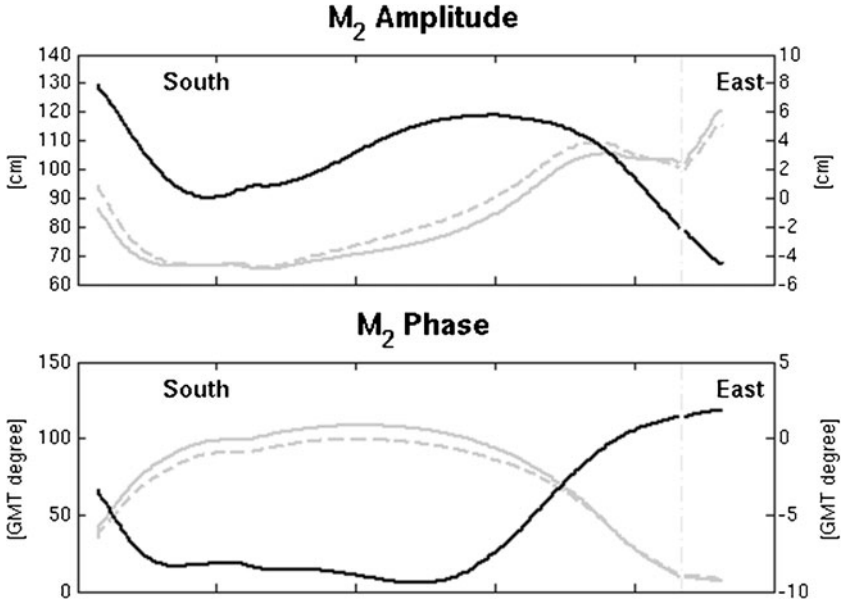

Fig. 4 Open boundary tidal amplitudes (*top panel*) and tidal phases (*bottom panel*) for M_2 tide along the model's two open boundaries from the south to the east. In each panel, prior estimate (*dash gray*), posterior (*solid gray*) are scaled by the *y*-axes on the left, while the refinement from data inversion (i.e., the difference between posterior and prior, in *solid black*) are scaled by the *y*-axes on the right. The *vertical line* (*dashed in gray*) shows the location where southern and eastern boundary intersects

To see how the inverse deduction helps to improve ROMS fitting, we provide for each station both observed and modeled M_2 tidal amplitude A and tidal phase Φ in Table 1. For side-by-side comparisons, tidal amplitude and phase are also transformed into complex tidal amplitude $Z = Ae^{-i(\pi/180)\phi}$, so that the model data misfit is quantified as the complex difference between observed (Z_o) and ROMS modeled (Z_m) (Davies et al. 1998; Lynch et al. 2004). Both "active" and "passive" stations are included in such comparisons to provide unbiased evaluation of the performance of the inversions. The mean complex misfits for prior, first inversion and the posterior are calculated for each tidal constituent to assess the overall effectiveness of data inversion.

It is found that about 50% reductions in observation/model misfits are achieved at 27 active stations, with mean misfit value reduced from 18.87 to 9.46 cm. As an independent validation, the observation/model misfits at 17 passive stations have similar reductions, indicating a seamless domain-wide solution improvement. Overall, the mean misfits for all 44 stations shows 44% misfit reductions for M_2 constituent in the Bohai and Yellow Seas area.

Comparing tidal co-amplitude/co-phase maps provides another means to diagnose the effectiveness of OBCs inversion adjustments in improving model interior solution (Fig. 5). Both the prior and posterior are validated against a recently published observational based M_2 cotidal map (Fang et al. 2004], which is grounded on both long-term coastal tide gauge and satellite altimetry data. Indeed, pronounced improvements in pattern agreement are found in the posterior solution. One good case is seen in the Bohai Sea, where the location and pattern of 0° phase line are greatly improved over the prior. Another significant improvement appears in the Bohai strait, where the 330° phase line is shifted westward in the posterior, providing better agreement with the observation. In the northern Yellow Sea, the tail of 270° phase line in the prior solution is located far to the east relative to the observation. This is improved again in the posterior. In the southern Yellow Sea, the prior posterior difference is not as obvious. Both provide similar results as the observational based cotidal map.

We conclude that the inverse tidal OBCs adjustments work well in significantly reducing the observation/model misfits. Model results derived from such a hybrid data assimilation method provide an optimal and dynamically consistent M_2 tidal simulation from which detailed tidal characteristics and dynamics can be gleaned.

5 Tidal characteristics

Given that ROMS, driven by refined OBCs now provides tidal solutions that agree well with observations, we use ROMS posterior solutions to further infer the tidal characteristics in the Bohai and Yellow Seas. The M_2 cotidal maps (Fig. 5) show the incoming M_2 tidal waves bifurcates at the southern open boundary, one branch moving toward the Shandong Peninsula and the other moving into the northern Yellow Sea. One part of the second branch continues moving into the Bohai Sea through the Bohai Strait. Interactions between incident waves and reflection waves from the land boundary lead to four amphidromic points in our study region: two in the Bohai Sea and the other two in the Yellow Sea. In the Bohai Sea, the amphidromic point located in the Liaodong Bay is in the proximity of Qinhuangdao, while the other one in the Laizhou Bay is in the vicinity of the Yellow River mouth. Together, they act like a quasi-degenerated system with their amphidromic points very close to the land

Table 1 M_2 harmonic constant: amplitude (Amp, in centimeter) and phase (Phs, in degrees refer to UT+8 Time) extracted from observations, ROMS prior, 1st inversion (1st Inv), and posterior (Post), respectively

M2	Observations		Prior		1st Inversion		Posterior		Model/Data Misfit		
Stations	Amp	Phs	Amp	Phs	Amp	Phs	Amp	Phs	Prior	1st Inv	Post
1	219.41	11.74	214.58	21.10	221.50	13.11	224.89	12.10	35.73	5.66	5.65
4	140.77	28.20	115.18	39.90	119.10	31.42	121.02	30.17	36.45	22.86	20.25
5	120.77	19.03	102.93	37.24	106.45	28.73	108.19	27.48	39.53	23.93	21.01
7	116.00	43.13	103.74	50.20	107.18	41.67	108.88	40.39	18.26	9.26	8.91
8	97.61	54.33	83.18	64.27	85.86	55.71	87.17	54.42	21.26	11.96	10.44
10	92.65	59.08	76.27	72.16	78.70	63.63	79.89	62.35	25.20	15.51	13.67
11	82.00	66.13	73.53	75.60	75.87	67.08	77.03	65.81	15.37	6.26	4.99
12	61.00	89.13	56.62	93.61	58.35	85.13	59.19	83.87	6.35	4.94	5.80
13	54.73	99.52	50.78	110.95	52.44	102.54	53.26	101.32	11.22	3.64	2.25
14	55.00	116.13	51.76	128.17	53.50	119.73	54.35	118.49	11.65	3.72	2.35
15	61.00	139.13	59.00	150.21	61.04	141.84	62.04	140.64	11.76	2.89	1.92
16	49.00	150.13	43.59	158.52	45.14	150.01	45.90	148.74	8.66	3.86	3.30
17	55.00	211.13	46.68	219.89	48.11	211.04	48.81	209.61	11.37	6.89	6.34
18	119.00	253.13	109.78	265.43	112.59	256.91	113.95	255.63	26.17	9.97	7.17
20	116.00	269.13	125.21	278.02	128.35	269.64	129.87	268.43	20.84	12.40	13.95
21	108.60	272.72	92.71	293.41	94.97	284.79	96.08	283.46	39.38	25.33	22.85
22	61.00	287.13	52.32	295.44	53.56	286.54	54.17	285.07	11.94	7.46	7.13
23	40.00	278.13	31.67	303.36	32.35	294.15	32.69	292.53	17.64	12.61	11.65
25	61.00	186.13	61.32	202.68	62.41	194.45	62.94	193.30	17.61	9.06	7.99
30	63.77	63.02	56.49	77.08	58.18	68.61	59.01	67.35	16.39	8.15	6.64
31	81.68	52.28	67.45	63.37	69.39	54.74	70.34	53.42	20.21	12.71	11.44
32	32.11	114.83	38.03	132.87	38.77	124.47	39.08	123.34	12.45	8.92	8.73
33	37.00	134.13	42.19	147.76	43.02	139.73	43.38	138.81	10.72	7.17	7.17
34	52.00	144.13	45.80	149.55	46.76	141.47	47.18	140.53	7.73	5.72	5.73
35	70.00	152.13	60.17	162.77	61.67	154.71	62.36	153.82	15.54	8.84	7.89
40	164.28	305.36	171.55	310.75	174.70	302.97	177.05	303.00	17.38	12.60	14.58
42	100.17	14.76	120.07	9.06	116.62	10.50	114.50	11.29	22.69	18.30	15.73
Mean misfits for active stations									18.87	10.39	9.46
2	140.75	14.20	122.47	23.53	126.75	15.14	128.86	13.94	28.12	14.17	11.91
3	134.77	30.52	116.63	37.32	120.61	28.85	122.56	27.60	23.46	14.64	13.85
6	121.16	27.15	101.07	36.23	104.54	27.72	106.25	26.46	26.65	16.66	14.97
9	91.00	57.13	73.43	63.29	75.76	54.72	76.90	53.43	19.64	15.64	15.10
19	113.00	263.13	119.73	275.59	122.76	267.18	124.23	265.95	26.14	12.83	12.65
24	29.78	132.14	33.55	155.69	34.34	147.47	34.72	146.34	13.44	9.68	9.36
26	100.45	215.18	106.04	220.35	107.81	212.30	108.66	211.23	10.86	9.03	10.91
27	19.20	102.03	19.46	115.75	20.06	107.90	20.34	106.95	4.63	2.19	2.04
28	45.70	53.80	43.87	74.35	44.86	65.95	45.35	64.72	16.08	9.62	8.67
29	60.32	61.38	52.05	75.81	53.57	67.35	54.31	66.10	16.33	8.98	7.64
36	88.40	169.30	93.89	181.16	97.51	173.05	99.15	171.98	19.61	10.96	11.61
37	144.47	289.01	144.30	293.72	146.91	285.82	148.80	285.81	11.87	8.48	9.25
38	152.84	289.22	143.06	293.60	145.65	285.70	147.52	285.70	14.95	11.65	10.64
39	168.87	299.01	163.59	302.83	166.59	295.01	168.81	295.03	12.29	11.91	11.71
41	49.18	261.02	44.83	296.65	45.29	288.75	46.07	289.08	29.06	22.95	23.29
43	87.77	17.04	103.14	12.00	101.74	13.34	100.49	14.14	17.50	15.25	13.58
44	104.99	268.02	94.58	271.96	98.40	263.93	100.23	262.91	12.47	9.79	10.31
Mean misfits for passive stations									17.83	12.02	11.62
Mean misfits for all stations									18.47	11.02	10.30

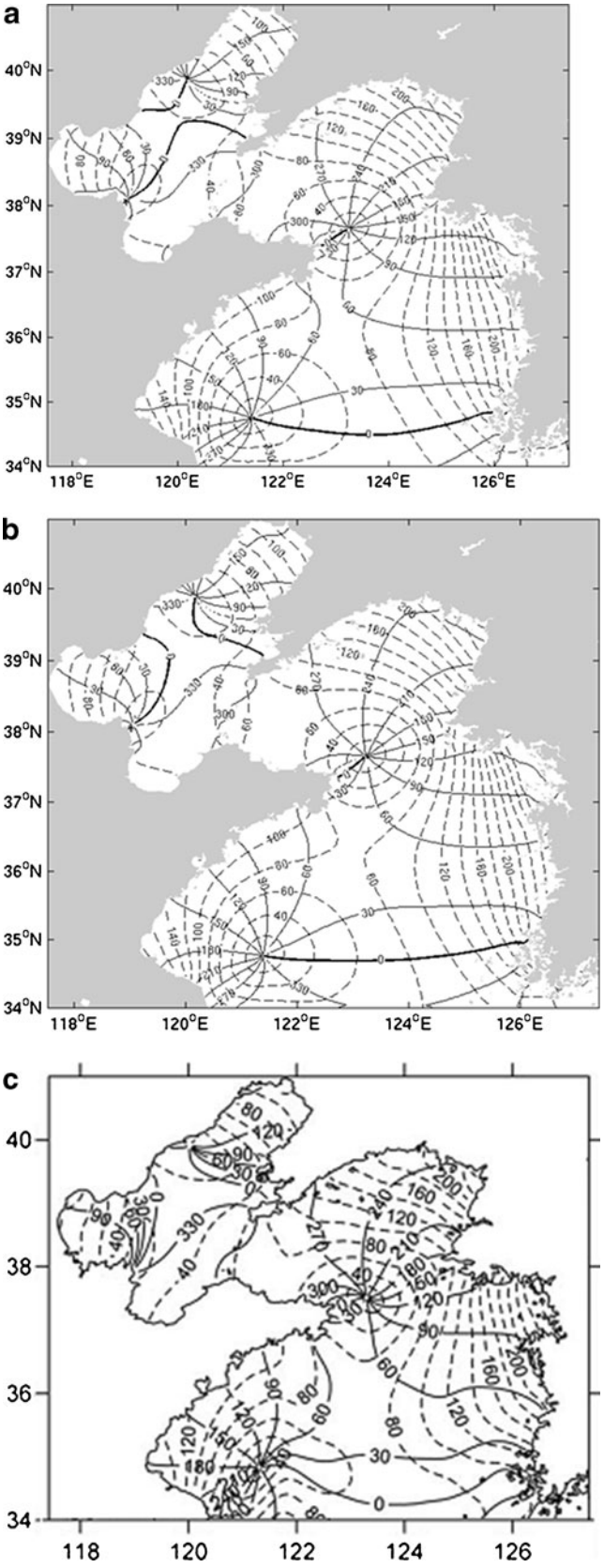

◀ **Fig. 5** M_2 cotidal maps from **a** ROMS prior solution and **b** ROMS posterior solution in comparison with **c** M_2 cotidal map constructed from the tide gauge and satellite observations by (Fang et al. 2004), taken as "ground truth" here. Tidal phase lag (in degrees with an interval of 30°) referenced to the UT+8 Time is shown in *solid contour lines*, whereas tidal amplitude (starts from 20 cm with an interval of 20 cm) are shown in *dashed contour lines*

boundary. In the Yellow Sea, the two amphidromic points are located at the northeast tip of Shandong Peninsula (Chengshantou) and outside of Haizhou Bay, respectively. It should be pointed out that the existence of amphidromic point in the Laizhou Bay is still in debate. Fang et al. (2004) argue this amphidromic point is further inland, while (Wang et al. 2004) using a nudging method shows the amphidromic point is in the similar location as our posterior solution shows. This region is in the Yellow River delta. Water bathymetry and coastline are both changing over time as a result of massive sediment transport of Yellow River, posing a challenge for accurate observation and modeling.

The largest M_2 tidal range is seen along the west coast of the Korean peninsula, especially in the middle area near Kyunggi Bay, where its maximum tidal amplitude exceeds more than 2.6 m. Off the Chinese coast, the tidal amplitude is relatively weaker, with its peak values of 1.4 m at the head of Haizhou Bay. Inside the Bohai Sea, M_2 tide is largely damped by the enhanced bottom friction associated with shallow bathymetry.

With ROMS' posterior solutions, the characteristics of tidal currents can be depicted by the depth-average tidal current ellipses (Fig. 6). In the Bohai Sea, the strongest tidal currents are seen in Liaodong and Bohai Bays with a maximum current speed of 0.6 ms^{-1}. The weakest current occurs in the Laizhou Bay with a speed of only 0.1~0.2 ms^{-1}. The tidal currents in the center of Bohai Sea behaves more like rotating currents rather than the rectilinear ones found in the Liaodong and Bohai Bays. In the Yellow Sea, the largest tidal currents are seen off the Korean coast with speeds ranging from 0.6 to 1 ms^{-1}. In contrast, tidal currents off the Chinese coast are only around 0.2~0.4 ms^{-1}. Near the center of south Yellow Sea, currents are also fairly weak with speed of ~0.2 ms^{-1}.

The ROMS' posterior solutions also show the west coast of Korea is dominated by rectilinear tidal currents, whereas the Chinese coast south of Shandong Peninsula is dominated by rotating tidal currents. In Yellow Sea, the rotation direction of tidal ellipses changes dramatically around 35° N, such that the rotation direction is predominantly clockwise south of 35° N, but becomes anti-clockwise north of 35° N, except in the coastal area south of Shandong Peninsula. This finding of tidal rotation direction change around 35° N is consistent with the previous observations (Lie et al. 2002) and modeled solutions (Kang et al. 1998; Lee and Jung 1999). The clockwise rotation south of Shandong peninsula is also confirmed by (Kang et al. 1998; Lee and Jung 1999; Lie

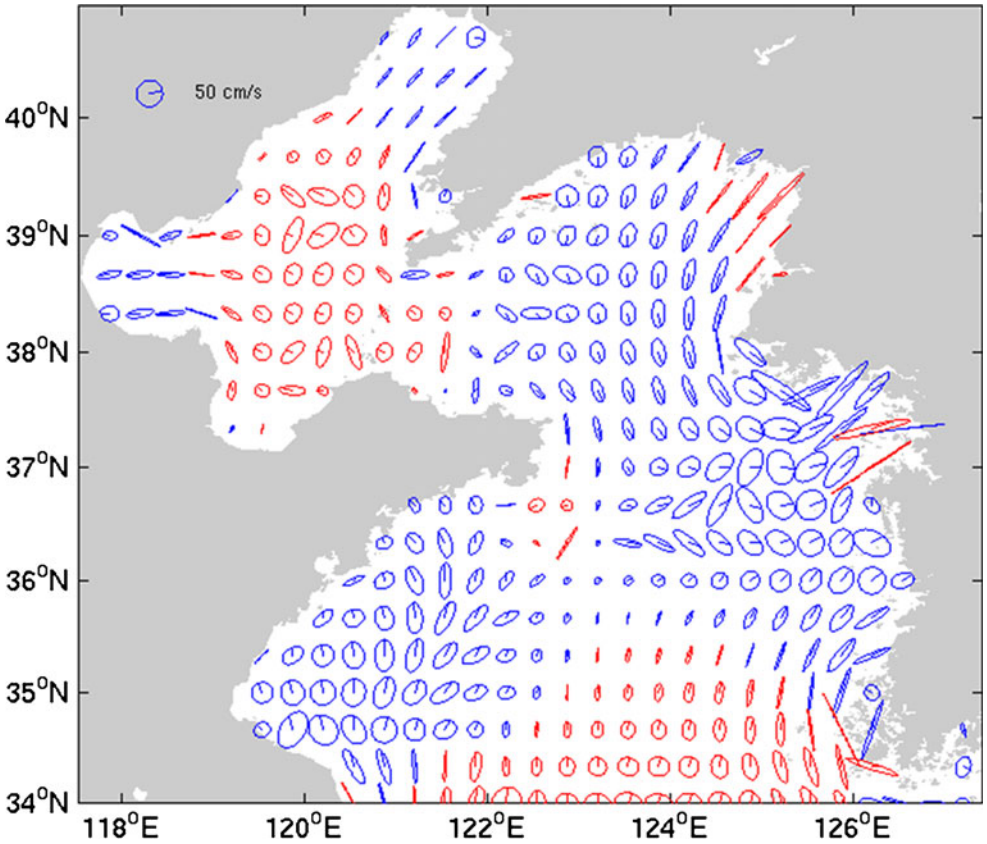

Fig. 6 Depth-averaged tidal current ellipses for M_2 constituent. Tidal ellipses are plotted every 10 grid points. The *blue* (*red*) represents the tidal ellipses rotate anti-clockwise (clockwise)

et al. 2002). In the Bohai Sea, the clockwise rotations are mainly seen in the center area while anti-clockwise rotations are present in the remaining area. We note all these results are in agreement with the theoretical prediction proposed by (Prandle 1982) that anti-clockwise current rotations are generally confined to regions with approximately constant spacing of co-range lines, such as in the northern Yellow Sea and south of Shandong Peninsula (Fig. 6).

6 Tidal dynamics and tidal residual circulation

To further explore tidal impact on the hydrodynamics in the Bohai and Yellow Seas, we now discuss the mixing property, residual circulation, tidal energy and its dissipation, as well as the momentum balance associated with M_2 tide.

6.1 M_2 tidal mixing parameter

One of our primary interests in the tidal response over this shallow region is to identify the contribution of tidal turbulence on generating mixing fronts. The locations of these tidal mixing fronts could be determined using critical vales of U^3/h proposed by (Simpson and Hunter 1974). Using the depth-averaged M_2 tidal velocity for U, we compute this tidal mixing parameter $\log_{10}(h/U^3)$ over the entire model domain, where h is the local water depth (Fig. 7). There are four regions of low values of $\log_{10}(h/U^3)$: the inner shelf of Seohan Bay, Kyunggi Bay, the shelf area off the southwest Korean peninsula, and the China shelf area between 34° N and 35° N. All these mixing zones are confined in the Yellow Sea. Earlier studies (Lie 1989; Naimie et al. 2001) suggest the critical value of $\log_{10}(h/U^3)$ of 2.0 to define the locations of tidal mixing fronts (Fig. 7), the contour of which highlights the areas where tidally induced vertical mixing plays a key dynamical role. Such mixing regions could be supported by relatively low temperature features often shown in satellite Sea Surface Temperature images (Hickox et al. 2000; Lie 1989). It should also be mentioned that those tidal mixing zones in reality can change due to mixing contributions of other tidal constitutes (e.g., diurnal tides) and buoyancy input from lateral boundary. For instance, vast fresh water discharge from the Yangtze River was reported to have negative influence on the mixing zones along the China Coast (Lie 1989), thus the shape and structure of these fronts can be different from time to time.

6.2 M_2 tidal residual circulation

Due to variable bathymetry, the tidal flow may generate residual currents through nonlinear interaction (Zimmerman

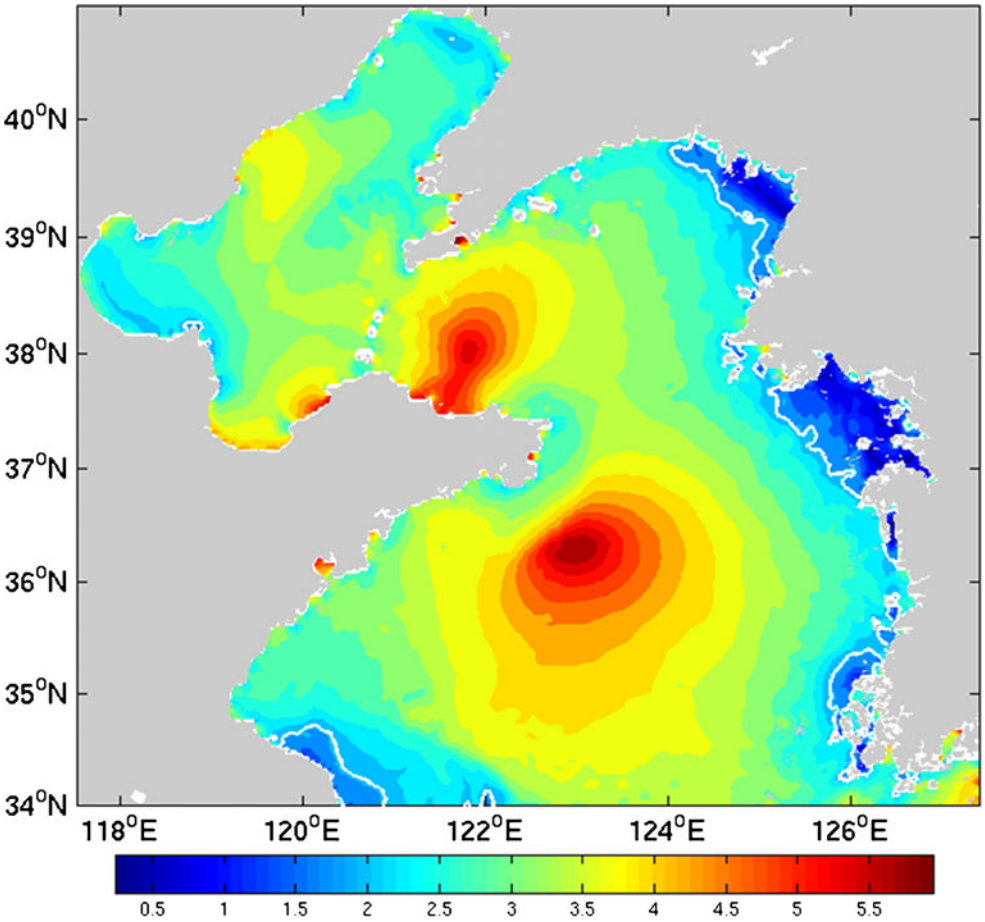

Fig. 7 Tidal mixing parameter $\log_{10}(h/U^3)$ for M_2 tidal currents, where h is the local depth in meter and U is the depth-averaged tidal velocity in meter per second. *Solid, white contour lines* indicate $\log_{10}(h/U^3)=2.0$, which defines the location of tidal mixing fronts

1978). Residual tidal currents in the estuaries and coastal zones have been recognized as a fundamental factor in determining long-term sediment and material property transport. To extract the time-averaged residual motion, the ROMS posterior M_2 tidal currents were averaged over a 12.42-h period. The residual currents (Fig. 8) in the interior of Bohai and Yellow Seas are rather weak, with speeds less than 2 cms^{-1}. Along the west coast of the Korean Peninsula, residual currents become stronger, reaching more than 5 cms^{-1}. Detailed examinations show that off the south tip of Liaodong Peninsula, there is a pair of anti-cyclonic and cyclonic headland eddies that may arise from the asymmetry of flood and ebb processes around this area. This result is consistent with the previous work of (Huang et al. 1999). Additionally, a weak, anti-cyclonic gyre can be found in the Laizhou Bay. Inside the Bohai Sea, strong residual currents are seen off the Yellow River mouth, near Liaodong Bay and north of the Bohai Strait (Fang and Yang 1985). Moving towards the Yellow Sea, the residual currents in the Yellow Sea interior primarily flow southward into the open ocean. Stronger residual currents are seen off the Chinese coast between 34° N and 35° N, inside the Seohan Bay, over the Kyunggi Bay, and offshore the southwest of the Korean Peninsula. These current patterns are also consistent with findings by (Lee and Beardsley 1999).

6.3 M_2 tidal energy and dissipation

Previous studies (Kantha et al. 1995; Munk 1997; Provost and Lyard 1997) point out approximate 8% of the total global M_2 energy is dissipated in the Yellow Sea regions. It is therefore meaningful to examine the detailed structures of barotropic tidal energy flux and its dissipations over this area. The mean tidal energy flux rate, consisting of both kinetic and potential energy, is calculated according to (Greenberg 1979):

$$F = \frac{\rho_0}{T} \int_0^T (h+\eta) \cdot \left[1/2 \cdot \left(u^2+v^2\right) + g\eta\right] \cdot (u + i \cdot v) \cdot dt,$$

where, ρ_0 is the density of seawater, taken as 1,026 kg/m^3, h is the local depth in meters, η is the sea level fluctuations due to tides, u, v are the depth-averaged tidal currents components from the posterior ROMS solutions and g is the gravitational acceleration, 9.8 ms^{-2}. The integration is

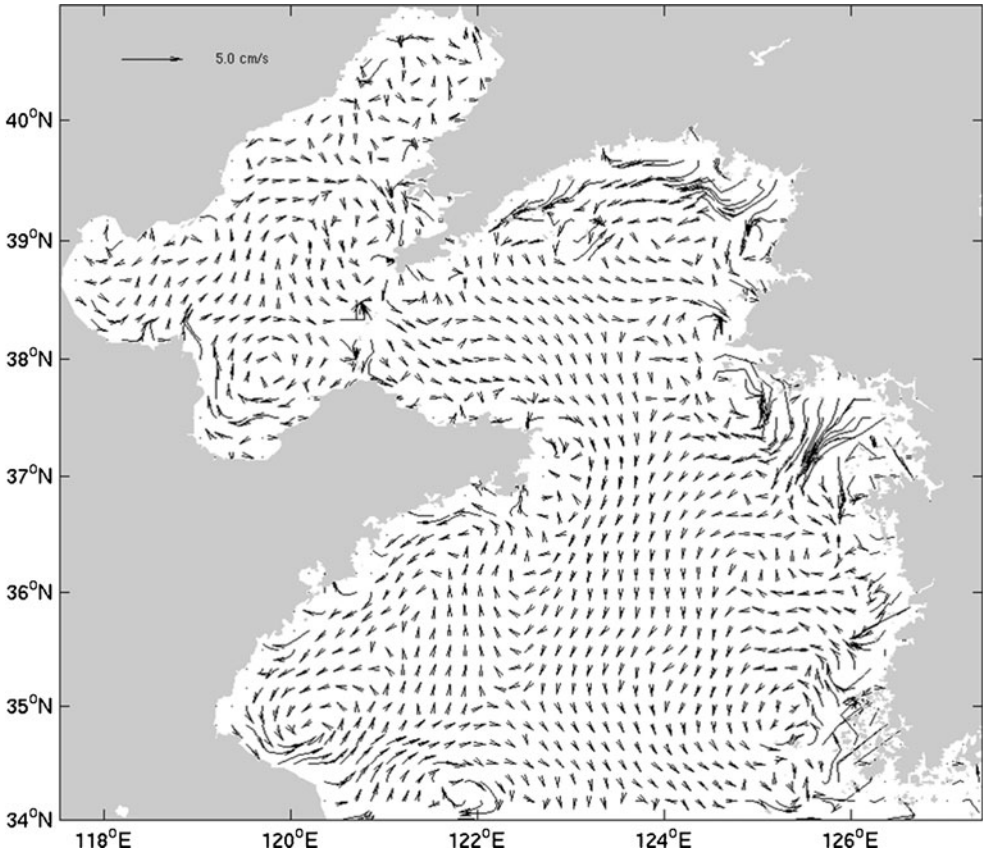

Fig. 8 Depth-averaged M_2 residual currents. The tidal residual vectors are plotted every 5 grid points

averaged over M_2 tidal period T (i.e., 12.42 h). The resulting mean tidal energy flux (Fig. 9) shows that the energy flux into our Bohai and Yellow Seas domain has two different sources: one through the southern open boundary and the other from the Cheju Strait at the eastern boundary.

A unique feature in the Yellow Sea is the asymmetry of tidal energy intensity—the energy flux passing through east of Yellow Sea trough is much larger than those west of Yellow Sea trough. The incoming tidal energy moves northward into the Yellow Sea and bifurcates around the 36° N, one small branch turning westward, while the main branch continuously moving northward. The former joins the southward energy flux south of the Shandong Peninsula and moves along the China coast toward the Subei shoals, forming a giant cyclonic gyre in the southern Yellow Sea. The main branch of energy flux moves further into the northern Yellow Sea and then turns westward following the land boundary, resulting in another cyclonic gyre in the northern part of the Yellow Sea. A small portion of tidal energy passes through the Bohai Strait (mainly the Laotieshan Channel). One branch turns northward into the Liaodong Bay and the remaining moves westward into the Bohai Sea interior. It is noted that along the Korean coast, massive tidal energy fluxes into the Kyunggi Bay, Seohan Bay, and the offshore areas southwest of the Korean Peninsula dissipate locally. These areas are significant sinks of regional tidal energy.

Mathematically, the tidal energy dissipation can be calculated following the scheme proposed by (Munk 1997; Taylor 1919):

$$D = \frac{1}{T} \int_0^T C_d \rho_0 \left(u^2 + v^2\right)^{\frac{3}{2}} dt,$$

where C_d is the bottom friction coefficient taken as 0.003 in our case, the other variables is the same as the abovementioned formula for tidal energy flux. This formula is based on the quadratic bottom stress scheme, which is consistent with our ROMS model configurations. The spatial pattern of mean tidal energy dissipation rate (Fig. 10) is consistent with previous studies of the tidal energy (Kang et al. 2002; Lefevre et al. 2000), showing the coastal areas along the Korean Peninsula are the largest energy dissipation sites in our domain. These areas have the strongest tidal currents as well as highly irregular bottom topography and coastlines. Specifically, we can identify three main areas of tidal dissipation using $\log_{10}D=0.3$ W/m^2 as the critical value. The largest dissipation rate is found inside the Kyunggi Bay with a maxima reaching up to 10 W/m^2. The other two are located near the head of Seohan Bay, offshore of southwestern tip of

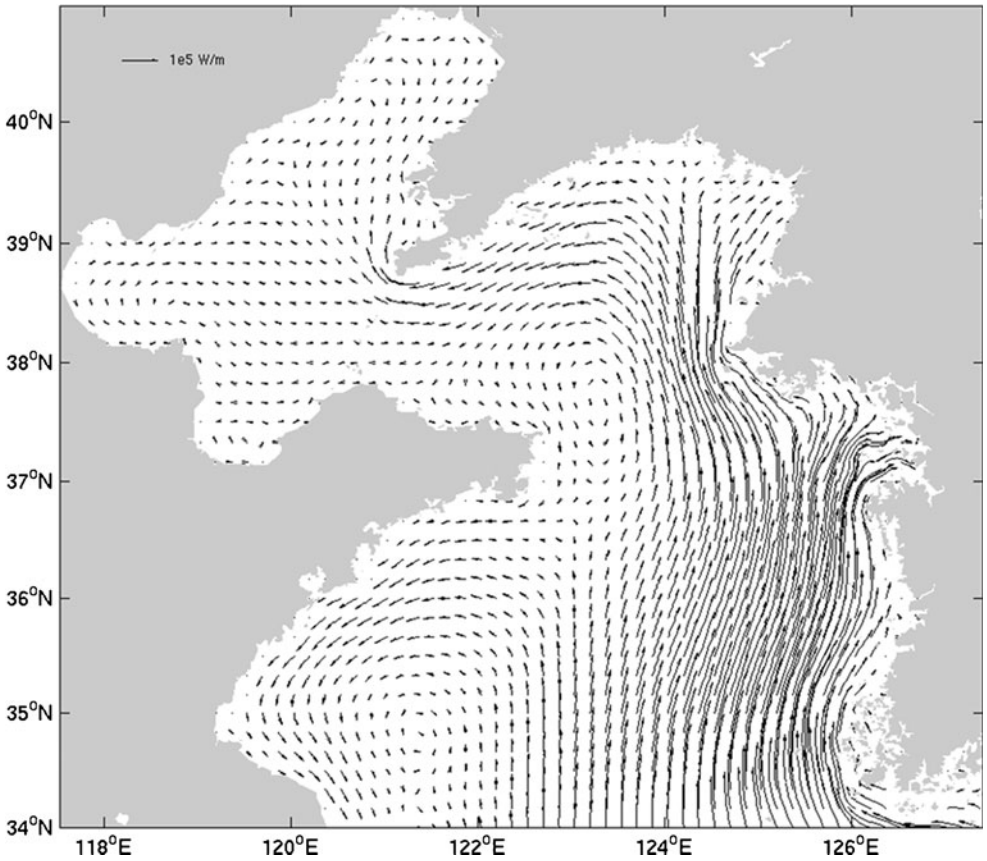

Fig. 9 M_2 mean tidal energy flux (unit, watt per meter), and the tidal energy flux vectors are plotted every five grid points

the Korean Peninsula, respectively. One common factor for these large tidal dissipation sites is that they all have much shallower topography and complex coastal geometry. Compared to coastal regions, tidal dissipation in the Bohai and Yellow Seas interior is negligibly small.

6.4 M_2 tides momentum balance

To get a more complete picture on regional tidal dynamics, we can further inspect the momentum balance of M_2 tide to piece out contribution of each physical process. Based on ROMS posterior solution, we analyze each of five terms in the depth-averaged momentum equation, including the local acceleration, horizontal advection, Coriolis force, pressure gradient force, and bottom friction. For both the U- and V-momentum equations, hourly time series of each term over the M_2 tidal period (12.42 h) are examined. Their standard deviations (Fig. 11) show the two largest terms are the local acceleration and pressure gradient terms, followed by Coriolis term. Although the Coriolis term is relatively weaker, it is still in the same order of magnitude of both local acceleration and pressure gradient terms, playing an important role in the formation of rotating tidal system. In most areas of the domain, horizontal advection and bottom friction are more than one order magnitude smaller, suggesting the nonlinear effects are rather weak. The exceptions are seen in several coastal areas such as Kyunggi Bay, where tidal current and the bottom frictions become much larger.

We can therefore divide our study domain into three areas: the weak dissipation zone, strong dissipation zone, and the intermediate dissipation zone. We can pinpoint a station in each of three zones to further illustrate the dynamical balance among different physical processes (see Fig. 1 for these stations A, B, C). Specifically, station A is selected in the interior of south Yellow Sea, around the 40-m isobaths south of the Shandong Peninsula. Station B is located in the middle of Bohai Bay at approximately 10-m isobaths, and station C is inside the Kyunggi Bay, with its depth of only 6 m. We examine hourly time series of each dynamical term in both U-momentum and V-momentum equations over 25 h (approximately two M_2 cycles), as shown in Fig. 12.

At station A, we see term balances that are typical in most areas of our study domain. In the U (east–west direction) momentum, the major balance is achieved among pressure gradient, local acceleration, and Coriolis terms, with the latter two terms acting in concert to balance the pressure gradient term. The magnitude of Coriolis term is smaller than the local acceleration term. Both bottom friction and horizontal advection terms are negligible. In the V (south–north direction) momentum balance, the situation is similar,

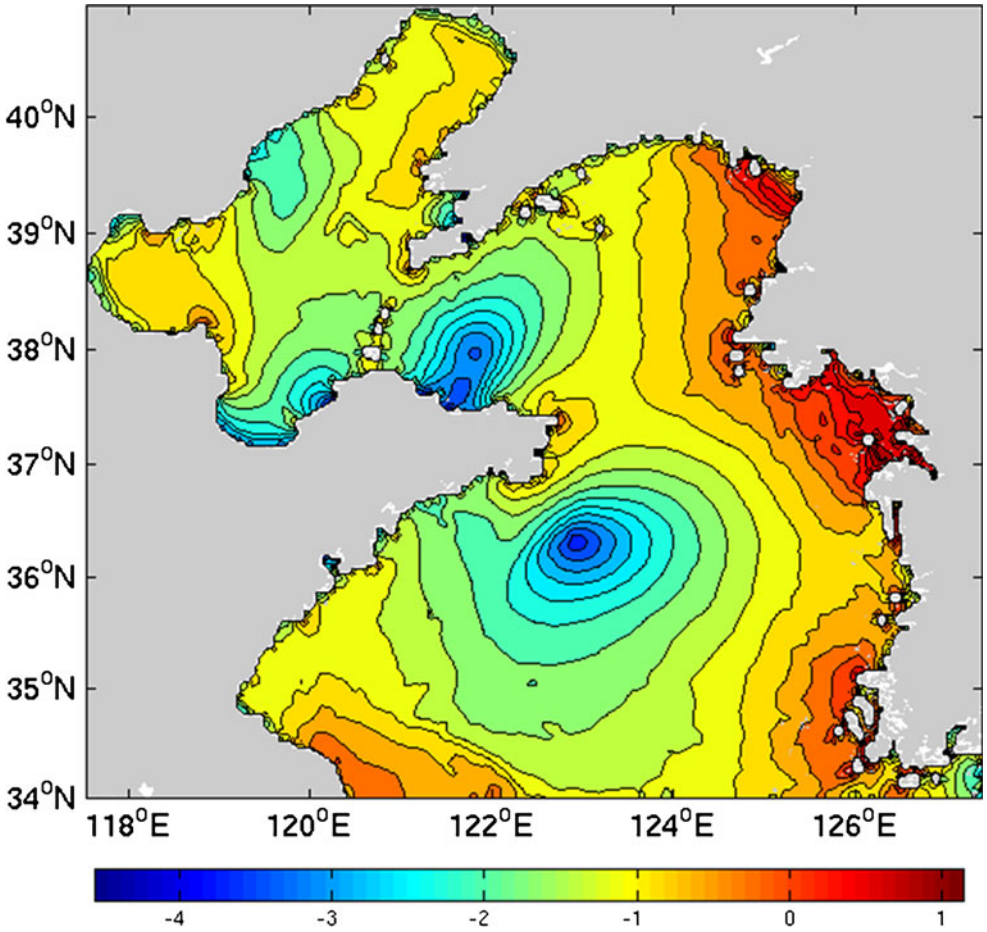

Fig. 10 M_2 mean tidal energy dissipation rate (unit, watts per meter squared). Values are scaled by $\log_{10}$

but now the Coriolis term increases to the same order of magnitude of local acceleration. This indicates tidal currents are stronger in the east–west direction, consistent with our previous discussions on regional tidal ellipse distribution. Contributions of both bottom frictions and horizontal advections remain negligible, suggesting the tidal dynamics in this local area is mainly linear.

Moving into the Bohai Bay, we see the dynamical balances are different at station B in that the contribution of bottom friction significantly increases at this site. In the U (east–west direction) momentum balance, the first two largest terms upon which the major balance is built are still the pressure gradient and local acceleration terms. The bottom friction becomes the third largest term to balance the residuals of pressure gradient and local acceleration. The Coriolis term becomes quite weak, having the same order of magnitude as the horizontal advection term. In the V (south–north direction) momentum balance, the major balance becomes geostrophic between the pressure gradient and Coriolis terms. The local acceleration is quite weak, and the bottom friction and horizontal advection become negligible again. This is expected considering the tidal currents at this site flow basically along east–westward, and there is very little V-component. Nevertheless, the increased importance of bottom friction (in U-momentum) suggests the tidal system at station B has already become nonlinear and dissipative.

Inside the Kyunggi Bay at station C, we can see a completely different dynamical picture. Due to the massive tidal energy around this region, each terms in the momentum balance become significantly larger than those at the other two sites (note the changes of y scale). The most striking feature in the momentum balance is that both the bottom friction and horizontal advection now increase to the same level of magnitude as the other terms. In the U (east–west direction) momentum balance, the largest two terms are the pressure gradient and bottom friction, followed by the local acceleration. The significant increase in the bottom friction and horizontal advection shows the nonlinear dynamics have already become important. We also see that the horizontal advection term has a period of M_4 tide, suggesting nonlinear generation of shallow water tidal constituent (M_4). Furthermore, we can see the bottom stress is approximately in the opposite phase with pressure gradient but lag by one hour, further confirming the importance of nonlinear dynamics. Considering the complex island geometry and topography around the Kyunggi Bay in conjunction with the massive tidal energy, it is not surprising to see such considerable increase in nonlinearity of the tidal

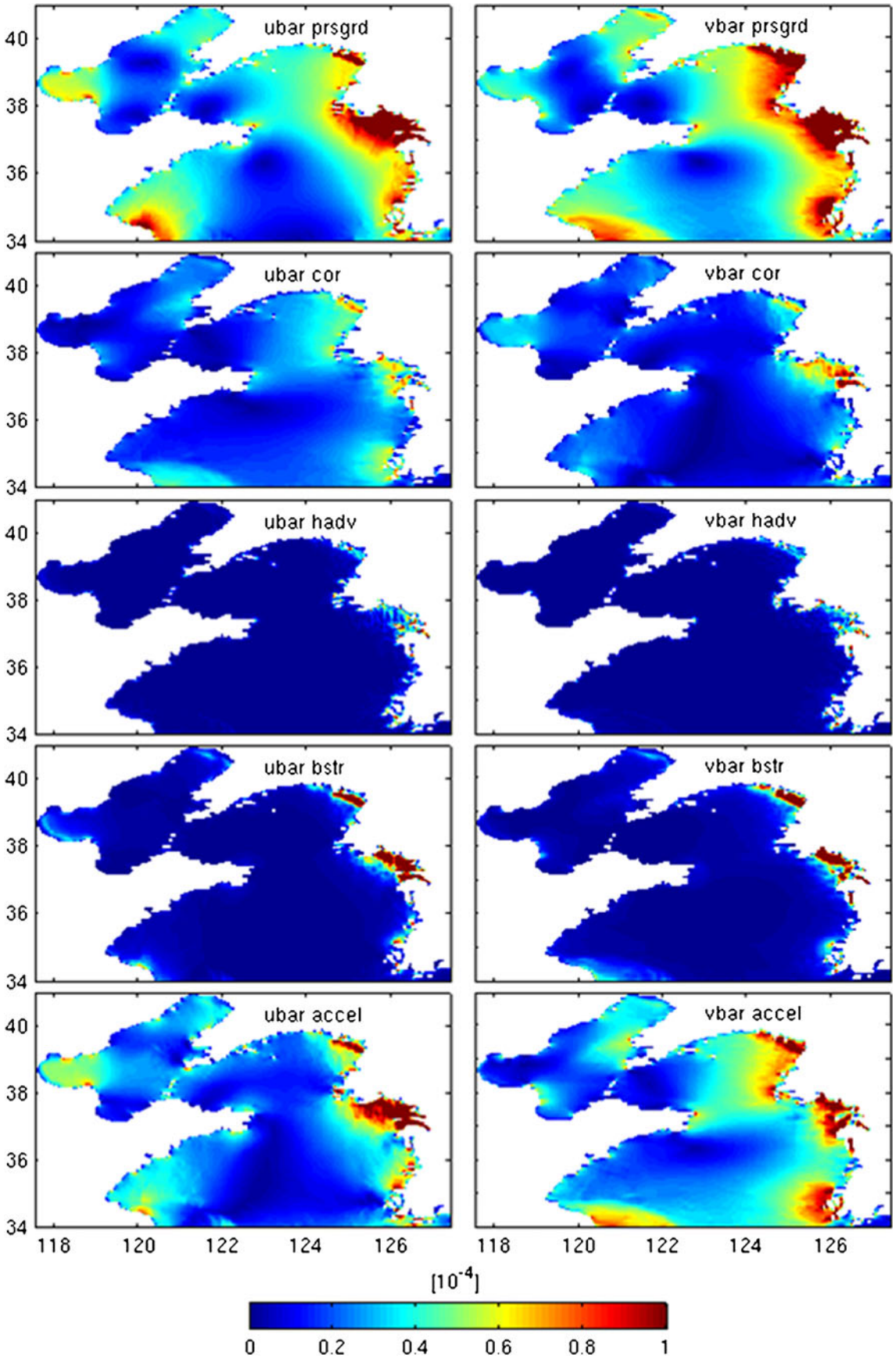
ubar prsgrd
vbar prsgrd
ubar cor
vbar cor
ubar hadv
vbar hadv
ubar bstr
vbar bstr
ubar accel
vbar accel
40
38
36
34
118
120
122
124
126
[10^-4]
0
0.2
0.4
0.6
0.8
1

◀ **Fig. 11** Standard deviations of depth-averaged dynamical terms in the U (east-west) and V (north–south) momentum equations over a M_2 tidal cycle, representing relative importance of each dynamical process. Term unit is in meter per second squared . *prsgrd*, *cor*, *hadv*, *bstr* and *accel* represent the pressure gradient term, Coriolis term, horizontal advection term, bottom friction term and local acceleration term, respectively

system. The dynamical balance situation is fairly similar in the V (north–south direction) momentum equation. The generation of shallow water constituent is very clear in the horizontal advection term, consistent with our previous analysis of tidal mixing and dissipation.

7 Summary and conclusion

We applied a high-resolution hybrid data assimilation modeling system to refine M_2 tidal simulation in the Bohai and Yellow Seas. The motivation of this work stems from the fact that tides and tidal currents are the dominant factors in the regional hydrodynamics. However, our knowledge of tidal characteristics and dynamics over this area are still hindered by limited observations that often suffer from the under sampling problem and errors in numerical model simulations that are constrained by quality and accuracy of OBCs. A common modeling practice is to obtain tidal OBCs from a global or basin-wide tidal model, which, however, is unable to resolve regional/subregional scale coastlines and topographic features due to coarse resolutions and topographic database being used.

The high-resolution hybrid data assimilating system applied in this study consists of a regional high-resolution ROMS as the forward model and TRUXTON as the inverse model. In situ tidal harmonics were assimilated via the incremental correction ("fine tuning") for the prior barotropic tidal OBCs. Because ROMS and TRUXTON use different model grids and numerical schemes, care was taken to allow these two models work in tandem. Model skill was evaluated by comparing the misfits between the observed and modeled tidal harmonics. This hybrid data assimilation approach is found very effective in correcting tidal OBCs, which in turn improves ROMS tidal solutions. Up to 50% decreases of model/data misfits are achieved after inverse data assimilation. It should be noted that because TRUXTON is a frequency domain model, it is therefore highly efficient in data inversion. Overall, this hybrid data assimilation approach provides a better alternative to the otherwise empirical "trial-and-error" way to tune-up regional tidal models. The utility of this hybrid data assimilating system has also been successfully demonstrated on the New England Shelf off the US east coast (He and Wilkin 2006).

One caveat of our hybrid inverse approach is in the underlying assumption that model/data misfits are the solo result of inaccurate specification of barotropic tidal OBCs,

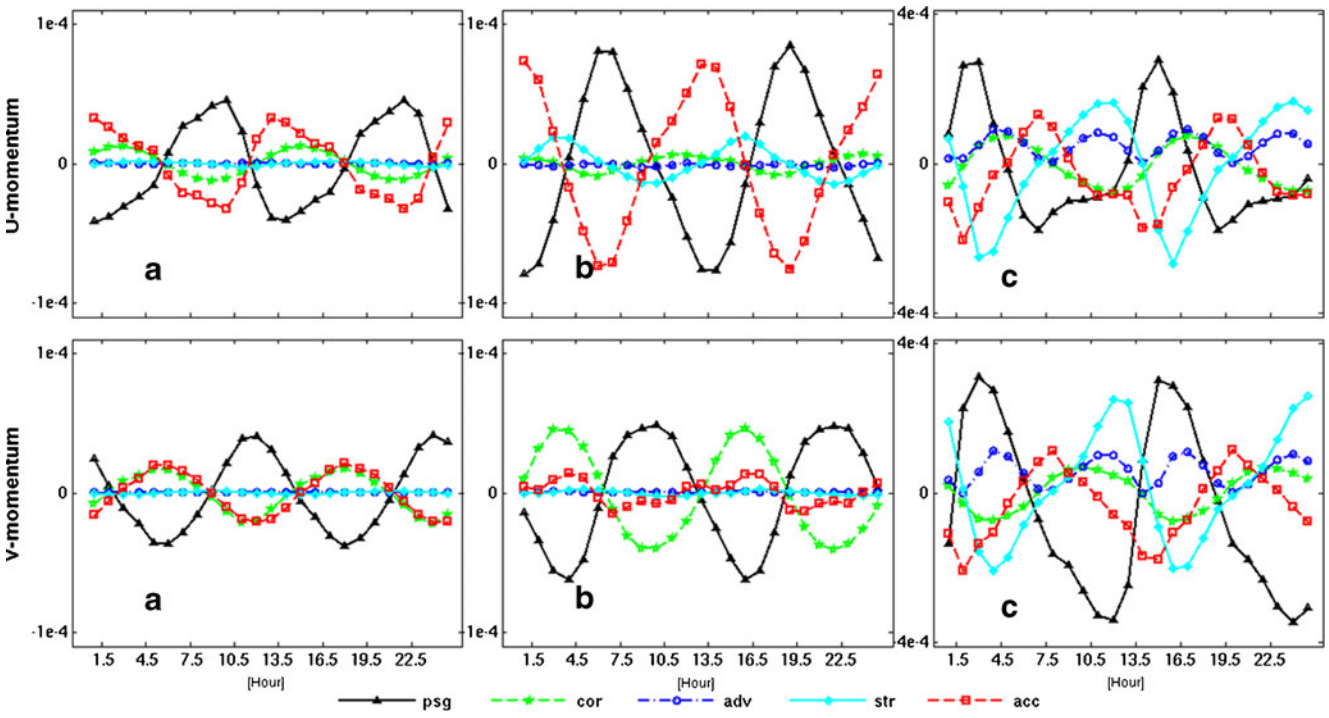

Fig. 12 A comparison of depth-averaged momentum balance in the east (u) and north (v) directions for the M_2 constituent at station A, B, and C (Fig. 1). The term unit is meter per second squared; *prsgrd*, *cor*, *hadv*, *bstr* and *accel* represent pressure gradient term, coriolis term, horizontal advection term, bottom friction term and local acceleration term, respectively

and that the error and covariance function (σ_η and w_0 and $\boldsymbol{w}_1$) can adequately account for misfit characteristics due to other processes. In reality, errors and uncertainties also arise from a variety of other sources, including errors in the observations themselves and model parameterizations such as bottom friction. With regard to the former, one needs to use accurate observations (and hence our decision to use sea level and pressures rather than current measurements in this study. Another reason for using pressure measurements is because the pressure fields have larger scales than do the current fields and thus are less subject to spatial aliasing of and internal tide contributions to current measurements). For the latter, more experiments may be needed in the future to explore model solution sensitivity to the frictional parameterization for which a more general inverse strategy is required.

The ROMS posterior solutions were used to generate M_2 cotidal map, which when compared to prior non-assimilation solutions, display significantly better agreement with the "ground truth" of (Fang et al. 2004). Our solutions show together there are four amphidromic points in the Bohai and Yellow Seas. Significantly larger tidal ranges are found along the west coast of the Korean Peninsula. Tidal current ellipse maps reveal an abrupt change in tidal rotation directions in Yellow Sea around 35° N, and that currents are the strongest on along the west coast of the Korean Peninsula, which combined with rough and irregular bottom bathymetry, produce significant tidal mixing and energy dissipation. Momentum balance analyses on M_2 further confirm the complexity of tidal dynamics in this area. For most regions in our study area, the main dynamical balance is between pressure gradient and local acceleration terms. Strong nonlinearity is present near the coast by virtue of enhanced bottom friction, horizontal advection, and the generation of shallow water tidal constituent (i.e., M_4), such that the dominant dynamical balance is achieved between the pressure gradient and bottom friction. This implies that a simple linear, analytical model will not adequately reproduce tidal currents and elevations.

References

An HS (1977) A numerical experiment of the M2 tide in the Yellow Sea. J Oceanogr 33(2):103–110

Aretxabaleta A et al (2005) Data assimilative hindcast on the Southern Flank of Georges Bank during May 1999: frontal circulation and implications. Cont Shelf Res 25(7–8):849–874

Bao X et al (2001) Three dimensional simulation of tide and tidal current characteristics in the East China Sea. Oceanol Acta 24 (2):135–149

Choi BH (1980) A tidal model of the Yellow Sea and the Eastern China Sea. Korea Ocean Research and Development Institute, Seoul

Choi BH et al (2003) A synchronously coupled tide-wave-surge model of the Yellow Sea. Coast Eng 47(4):381–398

Davies AM et al (1998) A three-dimensional model of wind-driven circulation on the shelf application to the storm of January 1993. Cont Shelf Res 18(2–4):289–340

Egbert GD, Erofeeva SY (2002) Efficient inverse modeling of barotropic ocean tides. J Atmos Ocean Technol 19(2):183–204

Egbert GD et al (1994) TOPEX/POSEIDON tides estimated using a global inverse model. J Geophys Res 99(C12):24821–24852

Fang G (1986) Tide and tidal current charts for the marginal seas adjacent to China. In: Zhou D (ed) Oceanology of China Seas. Kluwer Academic Publishers, Dordrecht, pp 101–112

Fang G (1994) Tides and tidal currents in East China Sea, Huanghai Sea and Bohai Sea. Oceanology of China seas 101–112

Fang G, Yang J (1985) A two-dimensional numerical model of the tidal motions in the Bohai Sea. Chin J Oceanol Limnol 3(2):135–152

Fang G et al (2004) Empirical cotidal charts of the Bohai, Yellow, and East China Seas from 10 years of TOPEX/Poseidon altimetry. J Geophys Res Oceans 109(C11):C11006

Flather RA (1976) A tidal model of the northwest European continental shelf. Mem Soc R Sci Liege 10(6):141–164

Foreman (1979) Manual for tidal heights analysis and prediction. Institute of Ocean Sciences, Patricia Bay

Greenberg DA (1979) A numerical model investigation of tidal phenomena in the Bay of Fundy and Gulf of Maine. Mar Geodesy 2 (2):161–187

Han G et al (2001) Optimizing open boundary conditions of nonlinear tidal model using adjoint method, ii: Assimilation experiment for tide in the Yellow Sea and East China Sea. Acta Oceanol Sin 23 (2):25–31

Hao W et al (2003) Tidal front and the convergence of anchovy (Engraulis japonicus) eggs in the Yellow Sea. Fish Oceanogr 12 (45):434–442

He R, Wilkin JL (2006) Barotropic tides on the southeast New England shelf: a view from a hybrid data assimilative modeling approach. J Geophys Res 111(C08002)

He R, McGillicuddy DJ, Smith KW, Lynch DR, Stock CA, Manning JP (2005) Data assimilative hindcast of the Gulf of Maine coastal circulation. J Geophys Res 110(C10):C10011. doi:10.1029/2004JC002807

Hickox R et al (2000) Climatology and seasonal variability of ocean fronts in the East China, Yellow and Bohai Seas from satellite SST data. Geophys Res Lett 27(18):2945–2948

Huang D et al (1999) Modelling the seasonal thermal stratification and baroclinic circulation in the Bohai Sea. Cont Shelf Res 19 (11):1485–1505

Hyun JH et al (1999) Tidally induced changes in bacterial growth and viability in the macrotidal Han River estuary, Yellow Sea. Estuar Coast Shelf Sci 48(2):143–153

Kang SK et al (1998) Fine grid tidal modeling of the Yellow and East China Seas. Cont Shelf Res 18(7):739–772

Kang SK et al (2002) Two-layer tidal modeling of the Yellow and East China Seas with application to seasonal variability of the M2 tide. J Geophys Res 107(C3):3020

Kantha LH et al (1995) Barotropic tides in the global oceans from a nonlinear tidal model assimilating altimetric tides: 2. Altimetric and geophysical implications. J Geophys Res 100(25):309–325

Larsen LH et al (1985) East China Sea tide currents. Cont Shelf Res 4 (1–2):77–103

Lee SH, Beardsley RC (1999) Influence of stratification on residual tidal currents in the Yellow Sea. J Geophys Res-Oceans 104(C7), 15, 615-679, 701

Lee JC, Jung KT (1999) Application of eddy viscosity closure models for the M2 tide and tidal currents in the Yellow Sea and the East China Sea. Cont Shelf Res 19(4):445–475

Lefevre F et al (2000) How can we improve a global ocean tide model at a regional scale? A test on the Yellow Sea and the East China Sea. J Geophys Res 105(C4):8707–8725

Lie HJ (1989) Tidal fronts in the southeastern Hwanghae (Yellow Sea). Cont Shelf Res 9(6):527–546
Lie HJ et al (2002) Computation methods of major tidal currents from satellite-trackeddrifter positions, with application to the Yellow and East China Seas. J Geophys Res Oceans 107(C1):3003
Lu XQ, Fang GH (2002) Inversion of the Tides on the Open Boundary of the BOHAI SEA by Adjoint Method. Oceanol ET Limnol Sin 33(2):113–120
Lu X et al (2009) Upwelling and surface cold patches in the Yellow Sea in summer: Effects of tidal mixing on the vertical circulation. Cont Shelf Res
Lynch DR, Naimie CE (1993) The M2 Tide and Its Residual on the Outer Banks of the Gulf of Maine. J Phys Oceanogr 23(10):2222–2253
Lynch DR et al (1998) Hindcasting the Georges Bank circulation. part I:: detiding. Cont Shelf Res 18(6):607–639
Lynch D et al (2004) Forecasting the coastal ocean: Resolution, tide, and operational data in the South Atlantic Bight. J Atmos Ocean Technol 21(7):1074–1085
Marchesiello P et al (2001) Open boundary conditions for long-term integration of regional oceanic models. Ocean Model 3(1–2):1–20
McIntosh PC, Bennett AF (1984) Open ocean modeling as an inverse problem: M2 tides in Bass Strait. J Phys Oceanogr 14(3):601–614
Munk W (1997) Once again: once again—tidal friction. Prog Oceanogr 40(1–4):7–35
Naimie CE, Lynch DR (2001) Inversion skill for limited-area shelf modeling. Part I: An OSSE case study. Cont Shelf Res 21(11–12):1121–1137
Naimie CE et al (2001) Seasonal Mean Circulation in the Yellow Sea - A Model-Generated Climatology. Cont Shelf Res 21(6–7):667–695
Ogura S (1933) The tides in the seas adjacent to Japan, Hydrographic Dept
Pawlowicz R et al (2002) Classical tidal harmonic analysis including error estimates in MATLAB using T_TIDE. Comput Geosci UK 28(8):929–937
Prandle D (1982) The vertical structure of tidal currents. Geophys Astrophys Fluid Dyn 22(1–2):29–49
Provost CL, Lyard F (1997) Energetics of the M2 barotropic ocean tides: an estimate of bottom friction dissipation from a hydrodynamic model. Prog Oceanogr 40(1–4):37–52
Shum CK et al (1997) Accuracy assessment of recent ocean tide models. J Geophys Res 102(C11), 25, 125-173, 194
Sikiric MD et al (2009) A new approach to bathymetry smoothing in sigma-coordinate ocean models. Ocean Model 29(2):128–136
Simpson JH, Hunter JR (1974) Fronts in the Irish Sea. Nature 250:404–406
Taylor GI (1919) Tidal friction in the Irish Sea. Proc R Soc London Ser A 96(678):330
Teague WJ et al (1998) Current and tide observations in the southern Yellow Sea. J Geophys Res-Oceans 103(C12), 27, 727-783, 793
Thomson RE, Emery WJ (2001) Data analysis methods in physical oceanography, 2nd and rev. ed. ed., 638pp., Elsevier, Amsterdam
Wang Y et al (2004) Tides of the Bohai, Yellow and East China Seas by assimilating gauging station data into a hydrodynamic model, in *Advances in marine science*, edited, pp. 253-274.
Xia C et al (2006) Three-dimensional structure of the summertime circulation in the Yellow Sea from a wave-tide-circulation coupled model. J Geophys Res Oceans 111(C11):C11S–C13S
Zhao B et al (1993) Numerical modeling on the tides and tidal currents in the Eastern China Sea, edited
Zimmerman J (1978) Topographic generation of residual circulation by oscillatory (tidal) currents. Geophys Astrophys Fluid Dyn 11(1):35–47
Zu T et al (2008) Numerical study of the tide and tidal dynamics in the South China Sea. Deep Sea Res Part I: Oceanogr Res Pap 55(2):137–154